THE JOURNAL OF PHYSICAL CHEMISTRY C

Article

pubs.acs.org/JPCC

Composite Ni/NiO-Cr_2O_3 Catalyst for Alkaline Hydrogen Evolution Reaction

Michael K. Bates, Qingying Jia, Nagappan Ramaswamy,† Robert J. Allen, and Sanjeev Mukerjee*

Northeastern University Center for Renewable Energy Technology (NUCRET), Northeastern University, Boston, Massachusetts 02115, United States

Supporting Information

ABSTRACT: We report a Ni−Cr/C electrocatalyst with unprecedented mass-activity for the hydrogen evolution reaction (HER) in alkaline electrolyte. The HER kinetics of numerous binary and ternary Ni-alloys and composite Ni/metal-oxide/C samples were evaluated in aqueous 0.1 M KOH electrolyte. The highest HER mass-activity was observed for Ni−Cr materials which exhibit metallic Ni as well as NiO_x and Cr_2O_3 phases as determined by X-ray diffraction (XRD) and X-ray absorption spectroscopy (XAS) analysis. The onset of the HER is significantly improved compared to numerous binary and ternary Ni-alloys, including Ni−Mo materials. It is likely that at adjacent Ni/NiO_x sites, the oxide acts as a sink for OH_{ads}, while the metallic Ni acts as a sink for the H_{ads} intermediate of the HER, thus minimizing the high activation energy of hydrogen evolution via water reduction. This is confirmed by in situ XAS studies that show that the synergistic HER enhancement is due to NiO_x content and that the Cr_2O_3 appears to stabilize the composite NiO_x component under HER conditions (where NiO_x would typically be reduced to metallic Ni^0). Furthermore, in contrast to Pt, the Ni(O_x)/Cr_2O_3 catalyst appears resistant to poisoning by the anion exchange ionomer (AEI), a serious consideration when applied to an anionic polymer electrolyte interface. Furthermore, we report a detailed model of the double layer interface which helps explain the observed ensemble effect in the presence of AEI.

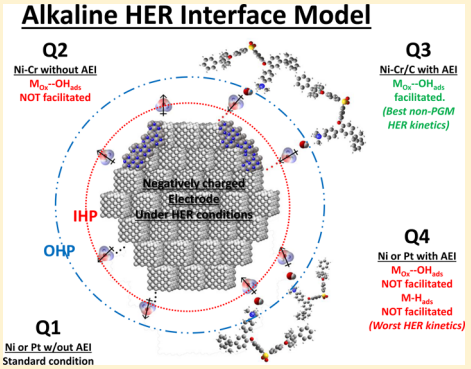

INTRODUCTION

Many researchers have envisioned "hydrogen highways" to supply hydrogen to a growing market of fuel-cell powered vehicles. A key challenge to the implementation of the hydrogen highways is the immense cost of building an infrastructure for the delivery and storage of hydrogen gas. However, the use of modular "plug & play" water electrolyzers significantly reduces the cost of this infrastructure because it allows market-driven deployment of individual refuelling stations. Although the cost of state-of-the-art water electrolyzers is significant, this cost is largely due to the use of the highly acidic proton exchange membrane (PEM)-based system which requires rare and prohibitively expensive platinum group metal (PGM) electrocatalysts. The requirement of PGM catalysts is a significant factor preventing the commercialization of this technology. This is especially relevant considering the order of magnitude higher loading of noble metals typically used in electrolyzers in comparison to concomitant application in fuel cells.[1,2] Alternative methods of hydrogen production such as high-temperature reforming of natural gas and methane produce very "dirty" reformate gases, which require complicated cleanup steps and reformate tolerant PGM catalysts in fuel cells to avoid catalyst deactivation from CO poisoning.[3−5] The development of alkaline electrolyzers circumvents the stability criterion restriction of the PEM systems and opens a pathway to utilize inexpensive and abundant first-row transition metal (TM) catalysts to produce pure H_2(g) via the direct electrochemical reduction of water. Although the inherent activity of TM electrocatalysts is much lower than PGM materials, the development of composite metal/metal-oxide interfaces may hold the key to unlocking the potential of PGM-free electrocatalysis.

Ni−Mo alloys have long been considered the most active non-PGM electrocatalysts for alkaline hydrogen evolution;[6−8] however, the inherent oxophilicity of the Mo component makes this material quite pyrophoric[7] and significantly complicates handling of the metallic alloy for use in any commercial device. Furthermore, a careful analysis of the Mo Pourbaix diagram indicates that metallic Mo exists only at potentials well negative of the HER onset. In fact, Mo has a small pH window where a passivation layer will form (near 0 V vs RHE between pH 4−8).[9] For pH values beyond this passivation window Mo tends to leach out of the metallic state, forming the MoO_4^{2-} oxyanion. Thus, while Ni−Mo electrodes have exhibited promising performance in PGM-free anion exchange membrane electrolyzers,[10] the long-term stability of Ni−Mo electrodes in this environment has not yet been demonstrated. In contrast, Ni−Mo films on Ni-mesh GDEs have shown long-

Received: December 10, 2014
Revised: February 14, 2015
Published: February 16, 2015

DOI: 10.1021/jp512311c
J. Phys. Chem. C 2015, 119, 5467−5477

term stability in an industrial application;[11] however the question of start-up and shut-down stability remains a significant issue for modular electrolysis systems where transient potential spikes could cause oxidation and subsequent dissolution of the Mo component of Ni−Mo alloys.

Although operation in an alkaline environment circumvents the stability criterion of PEM systems, one significant challenge of alkaline systems is the decreased hydrogen reaction kinetics.[12,13] In PEM systems, the direct involvement of highly mobile hydrated protons makes both the hydrogen oxidation and evolution reactions extremely facile, and the hydrogen electrode in fuel cell and electrolysis devices requires negligible overpotential to achieve operational current densities; this in the absence of strongly adsorbing anions is largely non-polarizable. However, in an alkaline environment, the source of protons for hydrogen evolution is no longer H_3O^+, but simply H_2O. Thus, the initial absorption of a proton to produce the H_{ads} HER intermediate requires much larger activation energy to strip a strongly bound proton from water than the E_a to remove H^+ from H_3O^+.[13,14] This phenomenon manifests in increased overpotential for hydrogen evolution (HER) and oxidation (HOR) required to achieve operational current densities with PGM electrocatalysts in alkaline electrolyzers compared to the PEM membrane electrode assemblies (MEAs). Supporting Information (SI), Figure S1 shows identical PGM electrodes tested in PEM vs anion-exchange membrane (AEM) MEAs and the resulting increase in cell overpotential for the AEM system compared to the PEM system, most of the contribution being a result of higher overpotential for HER.

A further complication of alkaline electrocatalysis results from the interfacial issues unique to the use of an anion-exchange ionomer (AEI) in contrast to the proton-exchange ionomer (most commonly, solubilized Nafion) used in PEM systems. The solubilized ionomer is intimately mixed with the catalyst layer (CL) during MEA fabrication. The presence of the ionomer helps to gradually extend the electrified interface deeper into the CL in a through-plane direction, thus increasing ionic conductivity and minimizing mass-transport limitations related to diffusion of the ionic species. In the case of Nafion, the SO_3^- moiety has been shown to interact with the catalyst, adsorbing onto the Pt surface,[15] but the effects of this adsorption on electrocatalyst performance are negligible, particularly in the HER region where the negative charge on the electrode surface electrostatically repels sulfonate species. The analogous ion-exchange group for OH^- transport in AEMs is typically the quaternary ammonium (QA) functional group. Although AEMs with QA functional groups show an optimized balance of stability (chemical and mechanical) and hydroxide conductivity compared to other anion exchange moieties,[16−18] the ammonium functionalities have recently been shown to poison Pt surfaces via electronic and/or covalent interaction and significantly inhibit electrocatalysis.[19] Here, we show that the anion-exchange functional groups in the ionomer do not result in loss of H_{upd}-derived electrochemical surface area (ECSA), but instead, the AEI affects the formation of HER intermediates, thus decreasing HER kinetics on Pt surfaces in alkaline electrolyte. In contrast, as we show in this report the Ni−Cr/C catalyst appears more resistant to inhibition by QA *vide infra*.

In this study we have screened a wide array of binary and ternary Ni-alloys and composite Ni/M_{Ox}/C (M_{Ox} = transition metal oxide) samples and have identified a composite Ni−Ni_{Ox}-Cr_2O_3 material as a front-line catalyst with performance rivalling that of state-of-the-art Ni−Mo. Furthermore, careful evaluation of the electrochemical response of benchmark Pt catalysts in the presence of acidic vs alkaline ionomer interfaces has provided a molecular level perspective of the interface. This work supports previous studies indicating synergistic enhancement of electrocatalysis on composite M/M_{Ox} surfaces and provides guiding principles for the development of non-PGM electrified interfaces for energy conversion and storage technology.

EXPERIMENTAL SECTION

Various binary and ternary Ni-alloy electrocatalysts were synthesized by a standard impregnation method using sodium borohydride reducing agent (Sigma-Aldrich). Ten millimoles of metal chloride or nitrate salts (Reagent grade, Sigma-Aldrich) were dispersed in 500 mL of H_2O (18.2 MΩ Millipore) and stirred for 15 min in a 1 L round-bottom flask. The carbon black support (Ketjen Black-EC600JD, Akzo Nobel Polymer Chemicals) was then added, and the reaction solution was stirred for at least 1 h. A total of 200 mL of freshly prepared 0.15 M solution (3 molar excess w.r.t. metals) of sodium borohydride (Sigma-Aldrich) was then added dropwise under vigorous stirring to chemically reduce the metal salts onto the carbon support. Upon addition of $NaBH_4$, bubbling was observed, and the solution changed color from a greyish suspension of carbon to dark black, indicating formation of nanoparticles. The solution was stirred for at least 1 h, vacuum-filtered through a Büchner funnel, and washed with 500 mL of DI H_2O. The solid product was dried in a vacuum oven overnight and then heated in a tube furnace at 500 °C for 6 h under 5%H_2/95%Ar forming gas to anneal the metal alloys. For comparison, the Ni/M_{Ox}/C samples were prepared by precipitation of M_{Ox} onto the carbon support, followed by $NaBH_4$ chemical reduction of Ni onto the M_{Ox}/C composite support and then subjected to the same sample workup (filtering, heating, etc.). The M_{Ox} precipitation was achieved by adding 1 M Na_2CO_3 (Sigma-Aldrich) dropwise until the solution changed to a gray or milky color and the solution pH was at least 10. The standard Pt catalyst was Pt black supplied by Proton On-site (Wallingford, CT). Other Ni-oxide and Fe-oxide catalysts referenced in SI, Figures S3 and S4, were purchased from QuantumSphere (Santa Anna, CA).

For rotating disk electrode (RDE) studies, inks composed of 5 mL of H_2O, 4.95 mL of 2-propanol and 50 μL of 5 wt % ionomer dispersion were mixed with an appropriate amount of catalyst. The ionomer dispersions used were either Nafion (perfluorosulfonic acid-PTFE copolymer, Alfa Aesar, Ward Hill, MA) or Tokuyama AS-4 (Tokuyama Co, Japan). The inks were sonicated for at least 30 min before a 10 μL aliquot was deposited on the tip of a polished glassy carbon disk (5.61 mm diameter) to produce a loading of 50 μg(metal)/cm^2. The catalyst layers were spin-coated on the RDE tip using an inverted Pine Instruments rotator to ensure uniform distribution of the catalyst. For examination of the ionomer effects on unsupported Pt black, the CL contained 250 μg(Pt)/cm^2 with a 5:1:1 mass ratio of catalyst/acetylene black (Chevron)/ionomer (i.e., 250 μL of 5 wt % ionomer dispersion in ink). Electrochemical tests were conducted with an Autolab (Ecochemie Inc., model PGSTAT30) potentiostat/galvanostat. Tests were conducted in a 100 mL jacketed three electrode cell using a water circulator (Neslab Exacal EX-300) to maintain 50 °C. Alkaline (0.1 M KOH) electrolyte was prepared using

DOI: 10.1021/jp512311c
J. Phys. Chem. C 2015, 119, 5467−5477

potassium hydroxide pellets (semiconductor grade 99.99%, Sigma-Aldrich). For each test, a freshly made RHE was used as the reference electrode, and a gold flag counter electrode was used to avoid Pt contamination. The glassy carbon WE was rotated using an RDE setup from Pine Instruments. Rotation rates of 2500 rpm were sufficient to remove the H_2(g) product from the surface of the WE and examine the kinetics well into the HER region. All results were obtained after conditioning electrodes with 50 mV/s CV scans (from 0 to 1 V for Pt, 0−0.5 V for Ni-alloys) for at least 20−30 scans, or until stable features were observed.

X-ray diffraction (XRD) characterization was conducted using a Rigaku Ultima IV XRD with a Cu Kα source (λ = 1.541 Å) operated at 40 kV and 44 mA. $2\theta/\theta$ scans were conducted using a 0.05° step size and 5 s hold per step. Scanning electron microscopy (SEM) characterization was conducted using a Hitachi S-4800 FE-SEM. EDS data were collected using EDAX Genesis on the SEM to validate sample elemental composition. High-resolution transmission electron microscopy (HR-TEM) images were collected on a JEOL 2010F TEM at 200 kV. X-ray absorption spectroscopy (XAS) measurements were conducted at the X3B beamline of Brookhaven National Laboratories, and analysis was performed using the IFEFFIT suite. Additional details of XAS measurements are provided in Supporting Information.

RESULTS AND DISCUSSION

The key challenges to efficient operation of alkaline electrolyzers and fuel cells are predominantly attributable to the hydrogen electrode reactions. While some researchers have claimed increased *kinetics* of the oxygen reduction reaction (ORR) in alkaline media,[20] the observed facility of ORR on various electrodes in alkaline media has more recently been explained in terms of stabilization of the ORR intermediates for outer-sphere electron transfer (often favoring the undesired 2 e^- ORR pathway).[21] For the oxygen evolution reaction (OER) in alkaline electrolyte, the onset potential and reaction kinetics appear to be favorable on many TM oxide electrodes[22,23] showing performance, which rivals PGM catalyst activity. In contrast, for the hydrogen electrode, non-PGM catalysts require large activation overpotential before the onset of the HER kinetic region. Ni-based catalysts have been reported as fuel cell anodes for the HOR in anion exchange membrane fuel cells (AEMFCs) and RDE studies but with very low activity.[24,25]

1. AEI Poisoning of Pt. High surface-area platinum is the benchmark catalyst for HOR/HER reactions, although Ir and Ru have also exhibited HOR activity in alkaline media.[26,27] As noted above, Pt suffers from two major challenges in alkaline media. First, the decreased HOR/HER kinetics in alkaline electrolyte related to the involvement of H_2O as the proton source as opposed to H_3O^+ in acidic media.[13] Second, the poisoning effects of the anion-exchange functional groups on Pt noted in previous work on the methanol oxidation reaction (MOR) in alkaline electrolyte by Kohl et al.,[19] which showed decreased hydrogen stripping charge on polycrystalline Pt electrode and decreased MOR current densities on bulk Pt and Pt/C in the presence of free quaternary ammonium species in the electrolyte as well as poly tetra-methylammonium hydroxide (their acronym PTMAOH is synonymous with the term AEI used here) ionomer deposited on the electrode surface. Here, we have further examined the interfacial phenomena on Pt/C and unsupported Pt black in the presence of an AEI binder as compared to Nafion binder during RDE testing. Interestingly, Figure 1 shows a negligible change in H_{upd}

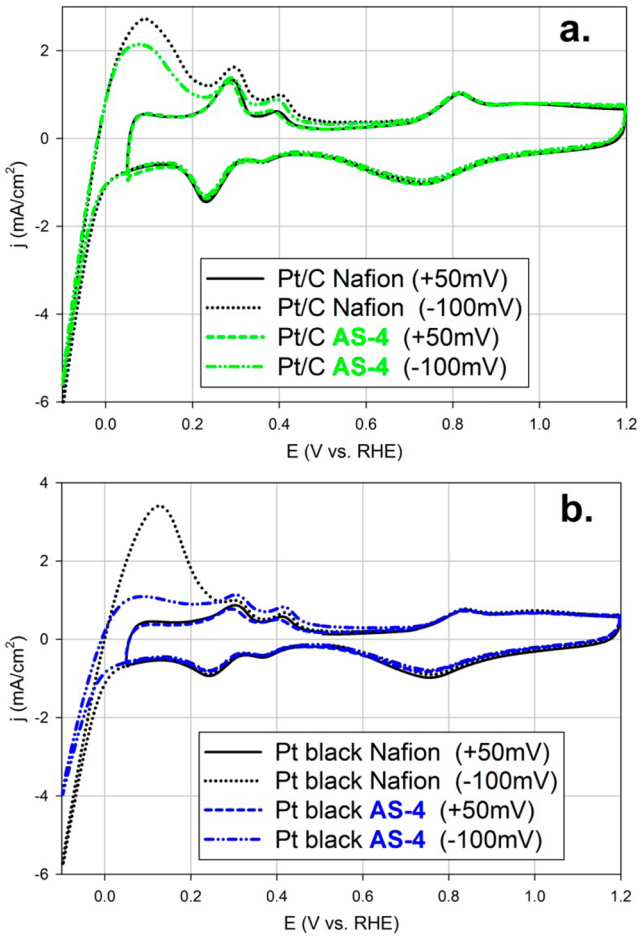

Figure 1. Diagnostic CV scans (50 mV/s) showing H_{upd} (+50 mV cathodic limit) and H_{opd} (−100 mV cathodic limit) on 50 $\mu g_{Pt}/cm^2$ Pt/C (a) and 250 $\mu g_{Pt}/cm^2$ unsupported Pt black (b) in the presence of Nafion vs AS-4 ionomer binders (incorporated during catalyst ink formulation). Scans collected in RDE cell with argon-purged 0.1 M KOH at 23 °C and 0 rpm.

charge in the presence of AEI. The H_{upd} is defined as the charge observed when the electrode is scanned in the potential range (vs RHE) from just above the thermodynamic standard reduction potential (+50 mV) to roughly the beginning of the double-layer region (+500 mV). The inhibitory effects of the AEI are only observed upon cycling to cathodic potential limits beyond the onset of the HER. This effect is observed upon cycling to cathodic potential limits of 0 V or −50 mV, but is most pronounced upon cycling to −100 mV (as shown in Figure 1). When scanning to potentials below the redox potential of the H_2O/H_2 couple (i.e., 0 V vs RHE), the electrochemical response is larger than the H_{upd} pseudocapacitive charge (as shown for various Pt surfaces in Figure S2) and is typically called "over-potential deposited" hydrogen (H_{opd}). The exact nature of this H_{opd} response is rather ambiguous. The "H_{opd} charge" may represent pseudocapacitance in excess of monolayer coverage from the adsorbed intermediate in the HER. The "H_{opd} charge" may also be interpreted as a superposition of H_{upd} pseudocapacitive charge and faradaic current produced from the oxidation of hydrogen formed in the cathodic scan below 0 V. In either case the charge

DOI: 10.1021/jp512311c
J. Phys. Chem. C 2015, 119, 5467−5477

observed in the anodic scan may not provide a suitable metric to accurately evaluate the ECSA of a Pt sample. Thus, the decreased "H_{opd} charge" does not represent a decrease in ECSA from specific adsorption of the QA moieties in the AEI, but rather a significant decrease in the HER activity in the presence of the AEI. In addition, Figures 1 and 2 clearly show particle-size effects on AEI adsorption. This is manifest in the difference of the HER and H_{opd} response of Pt black vs the supported Pt/C as shown in Figures 1 and S3. Difference in the ensemble size is manifest in the XRD analysis (Figure S4) of the two Pt samples and their calculated crystallite size (based on diffracting domains) indicating as expected a much smaller crystallite size for the supported Pt/C. The greater diminution of the HER and H_{opd} response in the presence of the AEI observed on Pt black compared to Pt/C suggests differences in the inhibitory characteristics of the AEI with reference to specific adsorption of QM moieties. In the presence of the AEI compared to the case with the Nafion binder, for scans with cathodic limits below 0 V vs RHE (As shown in Figures 1 and S3), the subsequent anodic peaks at ~300 and 400 mV are not changed as dramatically as the anodic response between 0 and 300 mV. This may point to a preferential blocking of the high index Pt(111) facets, typically attributed to the peak near 0 V.[28,29] This analysis supports the particle-size effect wherein Pt black with more bulk-like (hence predominance of (111) sites) is more severely effected as compared to Pt/C. While the details of the Pt/AEI interaction could be further elucidated with *in situ* spectro-electrochemical studies, the effect of HER/HOR inhibition on Pt surfaces in contact with AEI is clearly evident here. The decreased HER activity in the presence of the AEI binder is also seen in the HER CV scans on Pt catalysts in Figure 2 where the effect of the AEI on the well-dispersed Pt/C sample is comparatively smaller relative to the unsupported Pt black which exhibits substantial inhibition of the HER, as indicated by a ~20 mV shift in the half-wave potential on Pt black compared to ~5 mV shift for Pt/C.

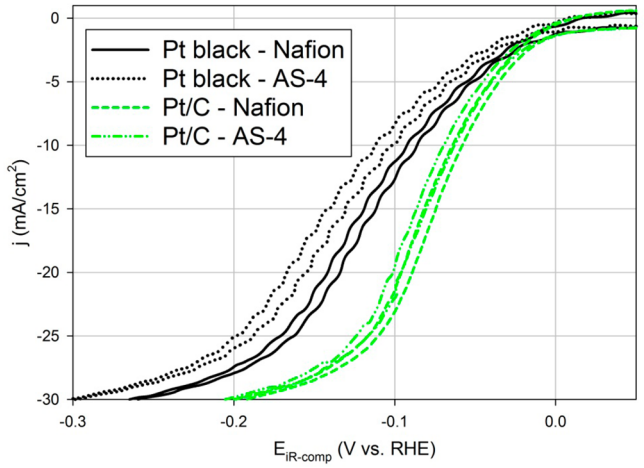

Figure 2. CV scans (50 mV/s) showing HER activity on Pt/C (50 $\mu g_{Pt}/cm^2$) and unsupported Pt black (250 $\mu g_{Pt}/cm^2$) in the presence of Nafion vs AS-4 ionomer binder. Scans collected in RDE cell with argon-purged 0.1 M KOH at 23 °C and 2500 rpm.

Aside from the apparent preferential blocking of the Pt(111) facets, the H_{upd} vs H_{opd} results in Figure 1 warrant a further clarification of the interfacial electrostatic effects of the AEI. In particular, Kohl et al.[19] surmised that the AEI likely resided in the inner Helmholtz plane (IHP) and exhibited a poisoning effect to decrease the ECSA and thus the MOR activity. This prior report evaluated the ECSA by scanning to potentials well below the onset of HER, thus observing the combined H_{upd} and H_{opd}. Furthermore, they did not make the distinction between H_{upd} and H_{opd} and thus concluded that the decrease in observed charge was due to poisoning of the catalyst ECSA via direct chemisorption of the AEI in the IHP. In this study, careful control of potential scan range indicates that the AEI likely straddles the double-layer interface such that some of the QM moieties reside in the IHP on Pt(111) surface sites, while the remainder of the QM moieties of the AEI reside in the OHP, not specifically adsorbed in the IHP. This residence of the AEI (in both IHP and OHP) also can account for the MOR results, where the electrode potential (φ_m) is positive of the potential of zero formal charge (PZFC), and thus the positively charged quaternary ammonium species on the AEI would be repelled by the positively charged electrode. It is more likely that the inhibitory effect of the AEI on MOR is related to the effective potential at the OHP (φ_2). In the case of MOR ($\varphi_m >$ PZFC) or HER/HOR ($\varphi_m <$ PZFC), φ_2 is more positive than it would be in the absence of AEI ($\varphi_2^{AEI} > \varphi_2$). As shown in Figure 3, for the relatively concentrated electrolyte used in this study, the Guoy–Chapman–Stern model of the double-layer interface predicts that the compact portion of the double-layer between the metal and the OHP will behave like a double-plate capacitor and exhibit a linear decrease in potential between the metal and the OHP.[30] Beyond the OHP, the model predicts an exponential decrease in potential from the OHP to the diffuse layer. On the basis of our analysis of H_{upd} vs H_{opd} above, it is likely that for MOR and HER/HOR conditions, the majority of the metal surface is still solvated by water molecules in the IHP. The effects of the AEI for the two situations are both related to the electrostatics exerted by the chemical potential of the AEI (μ^{AEI}) on the local environment. For the MOR, the AEI in the OHP creates a higher magnitude φ_2 which inhibits transport of OH^- from the OHP to the IHP. For MOR, the OH_{ads} is required to facilitate the removal of the CO_{ads} byproduct of the MOR as per the well-known Langmuir–Hinselwood mechanism for MOR. In contrast, the relative change in the effective potential at the IHP (φ_1) dictates the rate constant for the HER, as the reactant is the water solvent layer in the IHP. Thus, for the HER, the AEI exerts a similar dampening of the applied potential (φ_m) such that water molecules in the IHP experience a slightly less negative potential than they would in the absence of AEI ($\varphi_1^{AEI} > \varphi_1$ or, in terms of *magnitude* of negative charge: $|\varphi_1^{AEI}| < |\varphi_1|$). Thus, the decreased HER activity in the presence of the AEI can be accounted for by both specific adsorption on the high-index Pt(111) facets evidenced by the particle-size effects as well as the electrostatic effects which results in the H_2O HER reactants in the IHP experiencing a lower magnitude φ_1 in the presence of AEI than in the presence of Nafion.

2. HER Electrochemistry on Ni catalysts. Upon establishing benchmark HER performance with the Pt black catalyst, RDE testing was used to evaluate the kinetics of commercial samples of unsupported TM nanoparticles and numerous binary and ternary carbon-supported Ni-alloys. Investigations also included Ni catalysts deposited on composite metal-oxide/C supports including TiO_2/C, CeO_2/C, ZrO_2/C, WO_3/C, and Mo-Ox/C. Figures S5–S8, SI show the activity of many of the most promising Ni-alloy and Ni/Metal-Oxide/C samples. The best HER performance was

DOI: 10.1021/jp512311c
J. Phys. Chem. C 2015, 119, 5467–5477

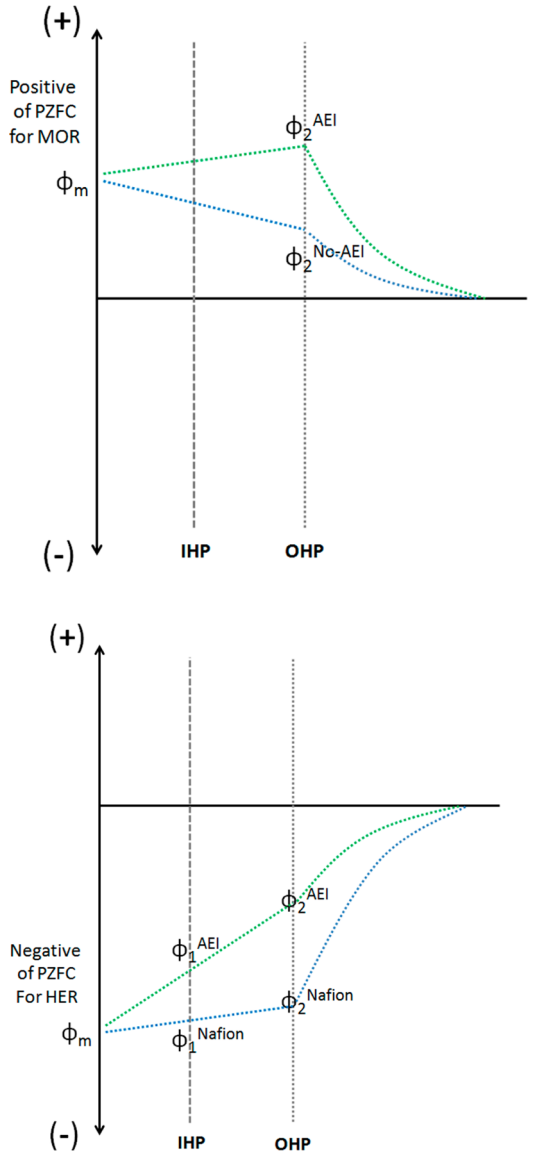

Figure 3. Qualitative representation of electrostatic effects of AEI on $\varphi 1$ and $\varphi 2$. The condition studied previously under MOR conditions[19] is represented in the top panel, while the condition studied in this paper is represented in the bottom panel. In both situations the chemical potential of the AEI (μAEI) increases the effective potentials at the IHP ($\varphi 1$) and the OHP ($\varphi 2$).

observed from a binary Ni−Cr/C sample with a 1:1 Ni/Cr atomic ratio. Figure 4 shows the steady-state HER performance of a Ni−Mo/C sample compared to the Ni−Cr/C and the Pt black benchmark. The performance of the Ni−Mo/C sample is typical for Ni-based catalysts in that it requires an overpotential (η) of 300−400 mV before the HER kinetic region is observed. This large overpotential has been attributed to a potential-dependent mechanism. The HER proceeds via three fundamental steps:

$$\text{Volmer: } H_2O + e^- \rightarrow H_{ads} + OH^- \text{ (electrochemical)}$$

$$\text{Heyrovsky: } H_{ads} + H_2O + e^- \rightarrow H_2 + OH^- \text{ (electrochemical)}$$

$$\text{Tafel: } 2H_{ads} \rightarrow H_2 \text{ (chemical)}$$

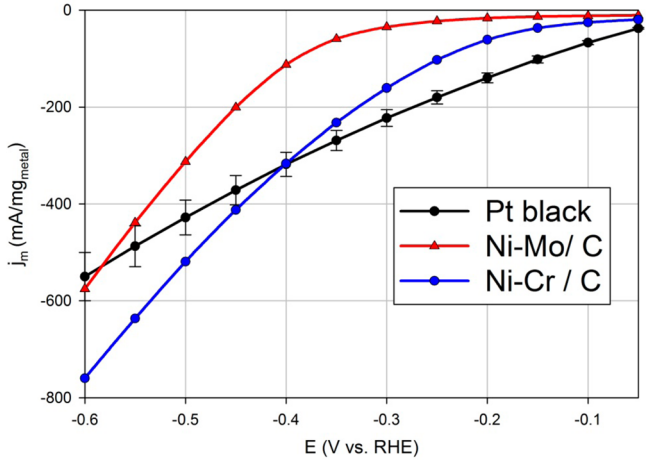

Figure 4. Steady-state HER chronoamperometry: 50 mV step size with 60 s hold-time/step in 0.1 M KOH (Ar-purged) at 50 °C and 2500 rpm. Catalyst loading is 50 μg(metal)/cm^2 with 15 wt % AS-4 used as binder in catalyst layer.

Previous literature has proposed that at low η the formation of the H_{ads} intermediate is the rds, and the reaction proceeds through a Volmer (rds)−Tafel mechanism, while at sufficiently high η, the surface is saturated by H_{ads} and the reaction proceeds via a Volmer−Heyrovsky (rds) mechanism.[6,8,31] However, a standard analysis of the kinetic mechanism from the Tafel slope is not possible because we cannot accurately quantify the active surface area of non-PGM catalysts. In addition, Tafel slope analysis is best conducted in the case of a planar electrode surface. But it is likely that this potential-dependent mechanism holds true for our nanoparticle systems—especially at the somewhat elevated temperature of the test conditions (50 °C) where the reverse of the Volmer reaction (desorption of H_{ads}) likely has a higher rate constant than the forward Heyrovsky reaction step, until sufficient η is applied such that saturation of H_{ads} is achieved.

While Ni does exhibit the most promising HER activity of any of the 3d TMs, it also suffers from deactivation via Ni-hydride formation.[32] Literature has shown that alloying Ni with other 3d TM elements helps to prevent the formation of Ni-hydride and increases the durability of the electrode.[33] Furthermore, Zhuang et al.[25] have theorized that decorating the Ni surface with Cr-oxide alters the electronic density of states of the Ni d-band in such a way to decrease the Ni−O bonding while retaining the Ni−H bond affinity. In addition, Jaksic has written extensively on the volcano plots for hydrogen binding energy and HER activity of numerous PGM and TM catalysts.[16,19] While this strategy of alloying Ni with other TMs has shown HER activity and inferred HOR activity on Ni-alloys, the literature generally shows large activation over-potential before the onset of the kinetic region of hydrogen electrocatalysis. Markovic et al.[27,34−36] have recently presented a new strategy to overcome the slow hydrogen kinetics in alkaline media via tailored metal/metal-oxide (M/M_{Ox}) interfaces. They have shown significant increases in HOR, ORR, and CO-oxidation performance by decorating Pt and Ni surfaces with TM-oxides. This strategy is similar to the spillover effects presented by Jaksic et al.,[37,38] for enhancing methanol, H_2/CO, and oxygen reaction kinetics on catalysts in which interactive hyper-hypo-d-electronic bonding occurs, and the formation of Pt−OH_{ads} species is substantially increased on catalysts supported on hydrated metal-oxides (Pt/Ta_2O_5−

DOI: 10.1021/jp512311c
J. Phys. Chem. C 2015, 119, 5467−5477

TiO_2/C or Pt/Nb_2O_5−TiO_2/C). In this configuration, OH_{ads} spills over onto the Pt sites to increase the turn over frequency (TOF) for CO-stripping, methanol oxidation, or ORR. We believe that, similar to the spillover phenomenon, adjacent M/M_{Ox} sites afford catalytic synergy to increase the effective TOF of the HER. As described by Markovic et al.,[14,27,34] the oxide site has an affinity to form OH_{ads}, thus weakening the H−OH bond in the HER reactant to allow for the formation of the H_{ads} HER intermediate on the metallic site. The large E_a of formation of the H_{ads} intermediate (Volmer reaction) is likely the cause of the lower hydrogen kinetics in alkaline vs acid media.

$$H_3O^+ + e^- \rightarrow H_{ads} + H_2O \text{ (acid)} \quad (1)$$

$$H_2O + e^- \rightarrow H_{ads} + OH^- \text{ (alkaline)} \quad (2)$$

The activation energy of reaction 1 is presumably much lower than for reaction 2. Although DFT studies have evaluated the energy of HER reactions in acidic media, the literature appears devoid of any computational studies comparing the E_a of reactions 1 and 2, likely due to the complications in accurately modeling the solvent and pH effects when attempting to quantify reaction energies in heterogeneous catalysis.[39] The large E_a of (2) can be lowered by weakening the H−OH bond. This can be achieved by carefully tailored surface sites with adjacent M/M_{Ox} components. Catalytic surfaces with nanoscale heterogeneity could offer a high density of adjacent M/M_{Ox} sites where the M site (metallic Ni^0) has an affinity for H-bonding, and the M_{Ox} (NiO_x) has a high affinity for OH_{ads} formation. Thus, as shown in the CV results in Figure 5, either

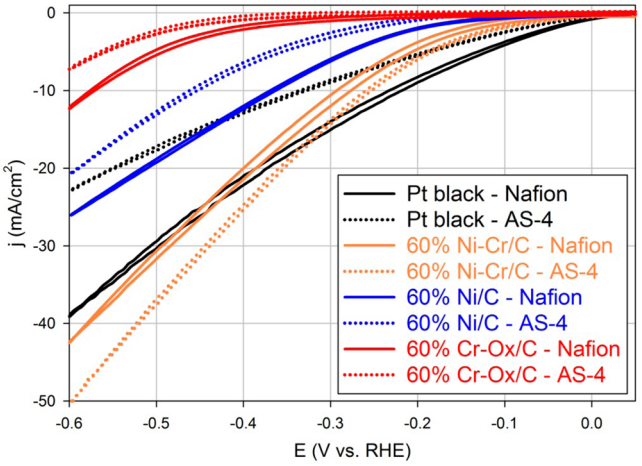

Figure 5. CV showing HER kinetics of Pt (black), Ni−Cr/C (orange), 60% Ni/C (blue), and 60% Cr-Ox/C (red) catalysts in 0.1 M KOH (Ar-purged) at 50 °C and 2500 rpm with Nafion vs AS-4 binder tested in RDE cell. Ni−Cr/C (orange) is the only sample that exhibits increased HER activity in the presence of AEI. All samples were prepared with 50 μg/cm^2 total metal loading.

the M or M_{Ox} surfaces alone require a large η to achieve kinetic-controlled HER behavior, while the composite M/M_{Ox} surface exhibits catalytic synergy for the HER and the M_{Ox} increases the HER TOF on the metal site. Figure 5 shows the HER CV results for Ni/C, Cr-Ox/C, and Ni−Cr/C compared to the Pt black benchmark (in the presence of Nafion vs AS-4 AEI). We observe that the Ni/C catalyst suffers from a large η before the kinetic region is established. The Ni/C sample is representative of a bare M surface (without M_{Ox}). It is well-known that metallic nickel electrodes are covered with a passivating surface oxide layer—NiO or $Ni(OH)_2$—when in contact with alkaline electrolyte. But this passivating surface oxide is electrochemically reduced at potentials below 0 V (vs RHE).[40] In fact, it is this passivating oxide layer that inhibits HOR on Ni electrodes. Thus, at potentials positive of the E^0 for HER, the Ni/C catalyst may actually be representative of the archetypal M_{Ox} surface, but upon applying a sufficient cathodic η to achieve HER kinetic-controlled behavior the Ni/C sample is representative of the bare M surface. The Cr-Ox/C sample exhibits negligible HER activity. This provides a baseline to show that the excellent HER activity on Ni−Cr/C is not simply the sum of HER from Ni and Cr-Ox components. In contrast to Ni/C and Cr-Ox/C the Ni−Cr/C sample achieves kinetic-controlled HER activity at very low η. Furthermore, Ni−Cr/C is in fact representative of a composite M/M_{Ox} interface as shown by XRD and *in situ* XAS analysis (*vide infra*). Thus, the results of Figure 5 support Markovic's theory of enhanced HER on composite M/M_{Ox} surfaces. For comparison, Ni−Mo nanoparticles were synthesized as per recent literature by Lewis et al.[7] and characterized using SEM (Figure S9) and HER CV scans (Figures S10−12). In addition to the low mass-activity of unsupported Ni−Mo catalyst samples, the Ni−Mo also exhibited decreased HER activity in the presence of AS-4 AEI (Figure S12). This indicates that while the d-band theory and volcano plots[31] have accurately predicted optimized H-bonding energy on Ni−Mo metallic surfaces, these surfaces do not exhibit the AEI-tolerance of the composite M/M_{Ox} materials.

3. Interfacial Studies on Ni Catalysts. In addition to the unprecedented mass activity, the Ni−Cr/C sample is the only sample that exhibits *increased* HER performance in the presence of the AEI binder, when compared to the HER activity in the presence of the Nafion binder. This apparent resistance to AEI poisoning is evident from the CV results in Figure 5. On the basis of the mechanistic models proposed by Lasia et al.,[6,8,41,42] this indicates that the AEI somehow inhibits formation of H_{ads} (Volmer reaction) on bare metals such as Ni or Pt, while on the composite Ni−Cr/C catalyst, the AEI appears to promote the formation of H_{ads}. On the basis of previous interfacial studies by Kohl et al.,[19] and the above discussion related to Figure 3, we can infer that the AEI exerts an electrostatic dampening of the negative charge on the electrode ($\phi_1^{AEI} > \phi_1$ or, in terms of *magnitude* of negative charge: $|\phi_1^{AE}| < |\phi_1|$). However, the *increase* in HER activity on the composite M/M_{Ox} interface of the Ni−Cr/C catalyst indicates that the AEI effects are not simply due to a dampening of the electrode charge. While the exact nature of the Ni−Cr/AEI interaction cannot be confirmed without further investigation such as using *in situ* spectro-electrochemical studies, we theorize that the AEI may affect the water dipole at the M/M_{Ox} interface. Scheme 1 details how the orientation of H_2O can facilitate formation of OH_{ads} on M_{Ox} sites (thus facilitating the alkaline HER rds: cleavage of the H−OH bond) or inhibit formation of H_{ads} on bare metal sites. Quadrant 1 (Q1) in the lower left shows the standard orientation of H_2O at the bare metal interface. In the standard orientation, the water dipole is oriented with the positively polarized hydrogen atoms pointed toward the negatively charged electrode. Q2 shows the M/M_{Ox} interface without AEI, where the orientation of H_2O makes it difficult to form OH_{ads} on the M_{Ox} site. We propose that the chemical potential of the AEI (μ^{AEI}) in the OHP decreases the magnitude of the electric field exerted on H_2O at the IHP (ϕ_1) thus allowing a

DOI: 10.1021/jp512311c
J. Phys. Chem. C 2015, 119, 5467−5477

Scheme 1. Proposed Interface Model for Alkaline HER on Pure Metal and M/M_{Ox} Surfaces[a]

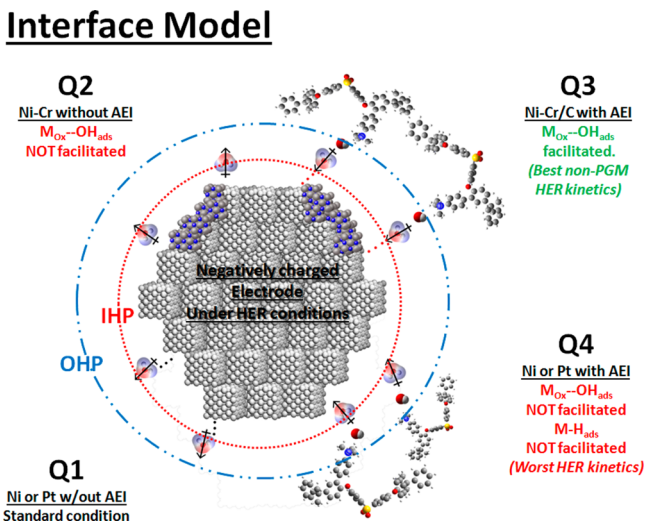

[a]AEI represented by archetypical quaternary ammonia polysulfone structure in OH-exchanged form. Metal represented by fcc unit cell model and metal oxide represented by NiO unit cell model.

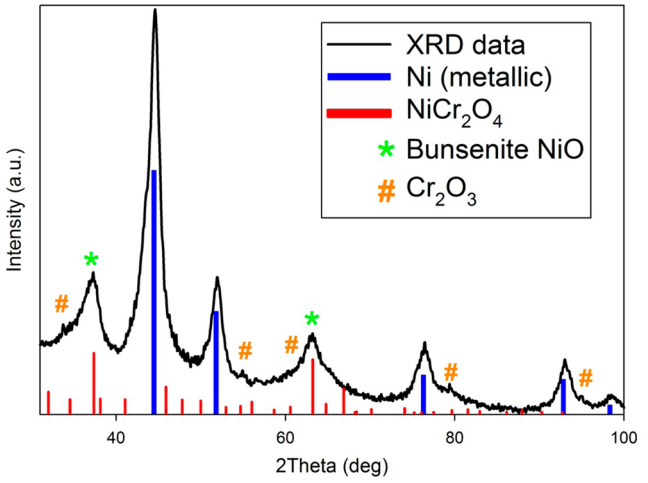

Figure 6. XRD of 60% Ni−Cr/C sample. $NiCr_2O_4$ is mixture of NiO and Cr_2O_3. Peak positions of standards retrieved from ICDD ref: 01-070-0989 (Ni), 01-085-0936 ($NiCr_2O_4$), 00-004-0835 (NiO), 00-006-0504 (Cr_2O_3).

greater fraction of the water solvent/reactant molecules in the IHP to orient their dipoles such that the hydrogen points toward the AEI, while the oxygen points toward the M/M_{Ox} interface—thus facilitating formation of OH_{ads} on the M_{Ox} site (Q3). The presence of M_{Ox} in close concert with bare metal surface benefits from these uniquely oriented water molecules, wherein the orientation of oxygen close to M_{Ox} provides for easy replenishment of the oxy-hydroxides. Closely juxtaposed, bare metals on the other hand have lower affinity to form hydrides in the context of the same orientation (Q4). Future studies involving the development of M/M_{Ox} catalysts for alkaline electrochemistry should be cognizant of the effects of ionomer on the interfacial electrostatics and solvent dipole orientation.

4. Characterization of Ni−Cr/C Structure and Composition - XRD. The high performance of the Ni−Cr/C catalyst was initially assumed to result from the alloying of Ni with Cr, which would presumably result in a change of the surface electronic structure. However, XRD and XAS studies show that even after heat-treatment at 500 °C under a reducing atmosphere, both the Ni and Cr components maintain some oxide character. EDS results (Figure S13) also support the presence of M_{Ox} components in the as-prepared sample. Figure 6 shows the XRD profile from the Ni−Cr/C catalyst. The metallic Ni peaks are the primary phase in the sample, but the wide peaks at 37 and 63° 2θ closely match the most prominent peaks in a $NiCr_2O_4$ phase. This nickel chromite spinel has recently been reported to form during the heating of NiO and Cr_2O_3 at 500 °C.[43,44] However, other reports did not observe formation of the $NiCr_2O_4$ phase until heating of NiO and Cr_2O_3 to 1200 °C.[45,46] The differences in the literature are due to the size of the precursor particles. Heating microparticles requires a much higher temperature to achieve phase transition to the mixed spinel phase, while mesoporous mixed metal oxides and metal oxide nanoparticles with much higher surface area and less long-range order allow for more rapid diffusion of the Ni into the Cr_2O_3 matrix—causing rearrangement to the spinel phase. However, the XRD data alone cannot definitively confirm whether the sample contains segregated NiO and Cr_2O_3 phases—or the spinel $NiCr_2O_4$ phase because of the similarity of the peak profiles for each system. The literature would suggest that the nanoscale of the material would allow for the low-temp formation of the $NiCr_2O_4$ spinel phase, but the profile fitting of Ni and $NiCr_2O_4$ phases requires a large skew in the Ni peaks—indicating that NiO phase is present in the sample. Nickel chromite has appeared in the literature as a catalyst for NO_x reduction[47] as well as benzene and CO hydrogenation.[48] So the spinel clearly has a high affinity for formation of gas phase H_{ads} in thermal reactors. Furthermore, the literature on metal oxide stability shows that Cr_2O_3 is one of the most difficult oxides to reduce as it exhibited no transition to metallic Cr in H_2-TPR studies up to 800 °C.[49] Thus, the sample likely contains a variety of metal oxide phases. To further investigate the Ni−Cr catalyst, we obtained *in situ* XAS data to analyze the chemical composition and atomic structure of the sample in contact with the alkaline electrolyte.

5. Characterization of Ni−Cr/C Structure and Composition - XAS. In an effort to reveal the structural origin of the high HER activity of the Ni-Cr/C sample, *in situ* XAS was performed on two Ni−Cr/C samples, comparing the sample with performance reported in Figures 4 and 5 with an alternative Ni−Cr sample exhibiting significantly lower activity. This comparison is used to illustrate the relative importance of moieties present on Ni and Cr surfaces and their role in the observed electrochemical response. The HER CV results for these two batches of Ni−Cr/C are compared in Figure S16. The samples were analyzed using 0.1 M KOH electrolyte with a specially designed cell (see Supporting Information) to determine the details of the changes to the coordination environments around Ni and Cr under *in situ* conditions. The electrodes were analyzed at various potentials from OCP = 0.8 V down to 0 V vs RHE. No significant changes in XAS data were observed for either Ni- or Cr-edges upon changing the applied potential; this is expected based on the lack of any redox changes predicted in Pourbaix diagrams or observed in CV results. Thus, the representative spectra collected at 0 mV is displayed in Figures 7 and 8 for discussion (attempts to collect data below 0 V vs RHE resulted in formation of H_2-bubbles on the "window" of the *in situ* cell, causing noisy spectra that could

DOI: 10.1021/jp512311c
J. Phys. Chem. C 2015, 119, 5467−5477

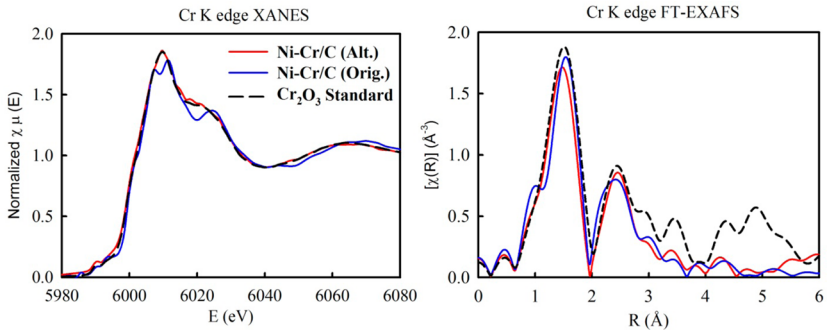

Figure 7. XANES (left) and FT-EXAFS (right) data at the Cr K edge collected on Ni−Cr/C electrodes. The data for Cr_2O_3 standard are also included for comparison purposes.

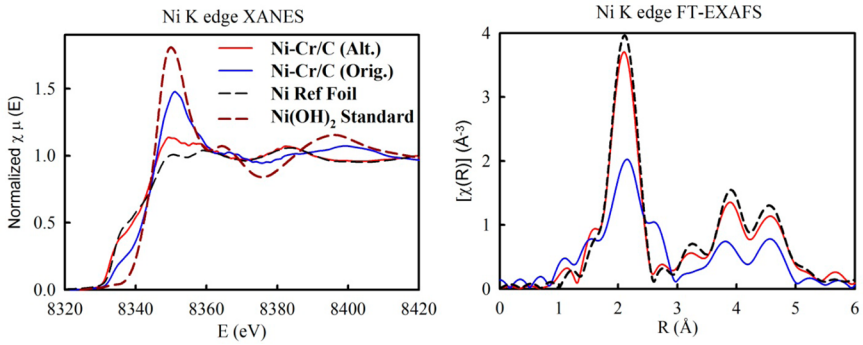

Figure 8. XANES (left) and FT-EXAFS (right) data at the Ni K edge collected on Ni−Cr/C electrodes. The XANES of $Ni(OH)_2$ standard is also included for comparison purposes.

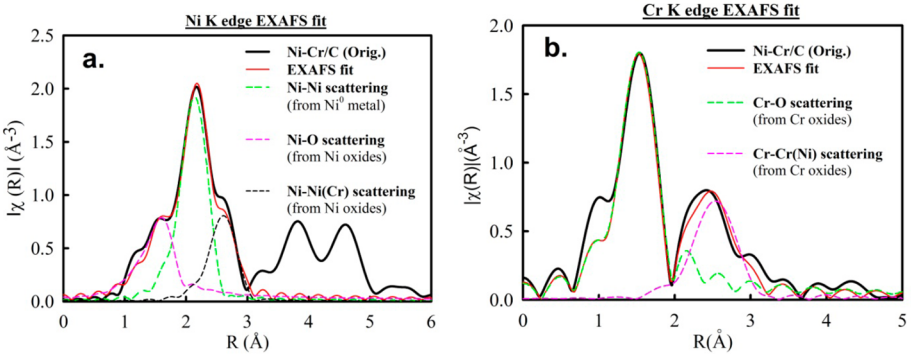

Figure 9. EXAFS fitting results from data collected from "original" Ni−Cr/C sample. Ni-edge fitting confirms mixture of metallic Ni^0 and Ni-oxide. While Cr-edge fitting excludes the presence of $NiCr_2O_4$ since the Ni−metal bond (2.98 Å) is in agreement with that in Ni-oxide (2.95 Å in NiO_x) but much smaller than the Ni−metal bond distance (3.42 Å) in $NiCr_2O_4$.

not be analyzed). Figure 7 clearly shows that the XANES and FT-EXAFS for the Cr K-edge of the two samples are essentially identical. In addition, the Cr-edge XANES spectra of the two samples are very similar to the Cr_2O_3 standard. The lack of fine details in the Cr_2O_3 XANES spectra of both samples compared to the reference indicates a lack of long-range order required to give coherent scattering profiles. Furthermore, the lack of prominent peaks in the FT-EXAFS beyond 3 Å compared to those of the Cr_2O_3 standard (Figure 7, right) indicates a lack of long-range order structure; i.e., the Cr_2O_3 exists as very small, nearly amorphous particles. The similarity of the Cr-composition for the high- and low-performance samples indicates that the Cr_2O_3 component is not providing the synergistic HER enhancement.

In contrast, the Ni-edge XANES and FT-EXAFS data for both samples are significantly different (Figure 8). The radial coordination environment shown by the Fourier transform of the Ni K edge shows the Ni−O interactions in the first peak (around 2 Å) followed by two specific Ni−Ni interactions between 3 and 5 Å. Ni K edge XANES also is in close concert with core level transition of s electrons and hence the electronic states near the Fermi level of Ni. Comparison of the Ni K edge XAS shows that while the alternate (poorly performing) sample exhibits only a slightly higher white line intensity at 8350 eV as compared to the reference Ni-foil, the original (high-performance) sample exhibits a much higher white line intensity, approaching that of the $Ni(OH)_2$ standard (Figure 8, left). This strongly suggests the presence of higher degree of Ni-oxides in the superior sample as compared to those present in the inferior HER sample. White line intensity is directly attributable to charge transfer from the Ni to the oxygen neighbors; hence a higher degree of oxides is directly related to the magnitude of

DOI: 10.1021/jp512311c
J. Phys. Chem. C 2015, 119, 5467−5477

the Ni−O interactions and hence peak magnitude. Consistently, the FT peaks of the inferior sample perfectly overlap those of the reference Ni-foil out to 5 Å with only slightly lower intensity, confirming the sample is dominated by metallic Ni (Ni^0). On the other hand, the original (high-performance) sample exhibits FT peaks at the same position as the Ni foil but with much lower intensity, as well as a distinct peak at ∼2.5 Å (without phase correction) that is not present in the inferior sample, indicating the multiple-component nature of the high-performance sample.

Analysis of Figures 7 and 8 indicates that the Ni/Ni_{Ox} surface behaves like Markovic's proposed archetypal M/M_{Ox} to provide synergistic HER enhancement. Thus, the Cr_2O_3 component likely stabilizes the Ni_{Ox} component under HER conditions where it would typically be reduced to Ni^0. As the XRD results in Figure 6 could not distinguish between the presence of $NiCr_2O_4$ and phase-segregated NiO and Cr_2O_3, EXAFS fitting was performed on the XAS data from the original (high performance) sample. Figure 9 shows the results of the EXAFS fitting which was conducted at the Ni and Cr K edges concurrently. The fitting details and results are given in Table S1. The fitting confirms that the peak at ∼2.5 Å (present on the original−but not the alternate sample) arises from the Ni−Ni scattering with a bond distance of 2.98 Å from Ni oxides (Figure 9, left). The Ni−Ni bond distance observed in the sample rules out the existence of the spinel $NiCr_2O_4$ phase in which the Ni−Ni scattering from Ni oxides would show a bond distance of 3.42 Å. Thus, the EXAFS fitting can definitively confirm the presence of phase-segregated NiO and Cr_2O_3, and exclude the presence of any significant quantity of $NiCr_2O_4$ phase.

The most significant difference in the XAS analysis of the two samples is that the original (high-performance) Ni−Cr/C sample exhibited a much larger NiO_x content which can be clearly seen in the much larger white line intensity and the FT peak at 2.5 Å in Figure 8. These results clearly indicate that the NiO_x and not the Cr_2O_3 must be responsible for the increased HER activity of the original sample. Thus, it may be that the amorphous Cr_2O_3 acts to stabilize the NiO_x, but does not appear to enhance HER activity directly. These data are supported by HR-TEM results (Figure S15) that appear to show a core−shell structure of Ni-NiO/Cr_2O_3 particles in the Ni−Cr/C sample. It is quite feasible that a porous Cr_2O_3 shell could stabilize the NiO component in the oxide state under HER conditions where the NiO would typically be reduced to metallic Ni^0. The stability of the composite M/M_{Ox} surface under HER conditions was observed in the stability of the HER performance during repeated CV cycling.

CONCLUSIONS

After screening of the HER activity of numerous binary and ternary Ni-alloys and composite $Ni/M_{Ox}/C$ materials, a Ni−Cr/C sample was identified that exhibits unprecedented mass-activity for the HER in 0.1 M KOH electrolyte. In particular, the Ni−Cr/C sample required the least amount of HER overpotential to achieve what literature indicates to be a direct Volmer−Heyrovsky mechanism. In addition, the effects of the AEI binder on the HER have been investigated for Pt, Ni−Cr, and Ni−Mo catalysts. For Pt catalysts, careful control of CV potential range limits indicates that the QM^+ moiety of the AEI likely straddles the double-layer interface and does not reside exclusively in the IHP. CV results from larger (∼6 nm) unsupported Pt black and smaller (∼2−3 nm) supported Pt/C catalysts indicates that at high-index Pt(111) surface sites, the QM^+ moiety of the AEI is specifically adsorbed in the IHP, while for other Pt(100) and (110) surface sites, the QM^+ moiety likely resides in the OHP, but still exerts an electrostatic effect, dampening the HER activity of the catalyst. Furthermore, the AEI inhibition of the HER is observed on Ni−Mo, but not on Ni−Cr/C. The cause of the AEI tolerance by Ni−Cr is not confirmed, but a model is proposed surmising that the AEI relaxes the dipole orientation constraints of H_2O in the IHP thus allowing more H_2O reactant molecules to assume an orientation which facilitates H−OH cleavage on adjacent M/M_{Ox} surface sites.

Various analytical techniques (XRD, EDS, XAS) have identified that the Ni−Cr/C sample actually contains metallic nickel as well as nickel- and chromium-oxides. XAS analysis of two different Ni−Cr/C samples indicates that the HER enhancement is related to the adjacent Ni/Ni_{Ox} surface sites and that the Cr_2O_3 phase may act to stabilize the Ni_{Ox} under the reducing HER conditions. The HER enhancement on composite Ni/Ni_{Ox} surfaces was observed by Lasia et al.[42] by cycling a polycrystalline Ni electrode from HER to OER conditions, thus roughening the surface with Ni_{Ox}, but the effects were not stable because the Ni_{Ox} was quickly reduced back to the metallic state under HER conditions. More recently, enhanced HER has been reported on Ni/Ni_{Ox} by Markovic et al.[34] and Gong et al.[50]—both of whom suggested that at adjacent metal/metal-oxide sites, the metal-oxide facilitates the formation of OH_{ads}, thus weakening the H−OH bond in the HER reactant and reducing activation energy for the Volmer reaction. However, the Ni Pourbaix diagram indicates that the Ni_{Ox} component of these composite surfaces is not stable below 0 V (vs RHE) and will quickly reduce to metallic Ni, thus losing the synergistic HER enhancement of adjacent Ni/Ni_{Ox} surface sites. All HER data in this paper was collected after confirming stable CV performance after at least 20 scans from −0.6 to +1.0 V (i.e., well before the onset of surface roughening under OER conditions). Thus, according to the XAS data shown here, it is likely that the Cr_2O_3 component stabilizes the Ni_{Ox} component well into the HER operating voltage, allowing the catalyst to retain the enhanced HER activity from synergistic Ni/Ni_{Ox} surface sites. Further studies of the effects of the workup conditions can be conducted to optimize the structure and activity of this M/M_{Ox} catalyst. This type of composite metal/metal-oxide electrocatalyst may be the key to realizing the promise of alkaline electrochemistry for low-cost, high-purity hydrogen production.

ASSOCIATED CONTENT

Supporting Information

Additional electrochemical analysis of HER cathode samples as well as XRD, EDS, SEM and TEM data. This material is available free of charge via the Internet at http://pubs.acs.org.

AUTHOR INFORMATION

Corresponding Author

*E-mail: s.mukerjee@neu.edu. Phone: 1-617-373-2382. Fax: 1-617-373-8949.

Present Address

[†](N.R.) General Motors Corporation, Global Fuel Cell Activities, 895 Joslyn Ave., Pontiac, MI, USA.

Notes

The authors declare no competing financial interest.

DOI: 10.1021/jp512311c
J. Phys. Chem. C 2015, 119, 5467−5477

■ ACKNOWLEDGMENTS

This work funded by the Advanced Research Projects Agency – Energy (ARPA-E), U.S. Department of Energy, under Award No. DE-AR0000121. We also thank Tokuyama Corp. For providing the AS-4 ionomer solution and Proton On-Site for providing the Pt black catalyst. Use of the National Synchrotron Light Source (Beamline X3B), Brookhaven National Laboratory, was made possible by the Center for Synchrotron Biosciences Grant P30-EB-009998, from the National Institute of Biomedical Imaging and Bioengineering (NBIB). Support from beamline personnel Dr. Erik Farquhar (X3B) is gratefully acknowledged. Special thanks to Dr. Wentao Liang for collecting HR-TEM data and to Samuel Boylston for his assistance in developing the figure for the interfacial model.

■ ABBREVIATIONS

AEI - anion exchange ionomer
AEM - anion exchange membrane
AEMFC - anion exchange membrane fuel cell
CL - catalyst layer
CV - cyclic voltammetry
ECSA - electrochemical surface area
FT-EXAFS - Fourier-transformed extended X-ray absorption fine structure
H_{upd} - underpotentially deposited hydrogen
H_{opd} - overpotentially deposited hydrogen
HER - hydrogen evolution reaction
HOR - hydrogen oxidation reaction
IHP - inner Helmholtz plane
MEA - membrane electrode assembly
M/M_{Ox} - metal/metal-oxide
MOR - methanol oxidation reaction
OCP - open-circuit potential
OER - oxygen evolution reaction
OHP - outer Helmholtz plane
ORR - oxygen reduction reaction
PEM - proton exchange membrane
PGM - platinum group metal
PZFC - potential of zero formal charge
QM - quaternary ammonium
RDE - rotating disk electrode
RHE - reversible hydrogen electrode
rds - rate-determining step
TOF - turnover frequency
TM - transition metal
XAS - X-ray absorption spectroscopy
XANES - X-ray absorption near-edge spectra
XRD - X-ray diffraction

■ REFERENCES

(1) Carmo, M.; Fritz, D. L.; Mergel, J.; Stolten, D. A Comprehensive Review on Pem Water Electrolysis. *Int. J. Hydrogen Energy* **2013**, *38*, 4901–4934.
(2) Kriston, A.; Xie, T.; Popov, B. N. Impact of Ultra-Low Platinum Loading on Mass Activity and Mass Transport in H_2-Oxygen and H_2-Air Pem Fuel Cells. *Electrochim. Acta* **2014**, *121*, 116–127.
(3) Urian, R. C.; Gullá, A. F.; Mukerjee, S. Electrocatalysis of Reformate Tolerance in Proton Exchange Membranes Fuel Cells: Part I. *J. Electroanal. Chem.* **2003**, *554–555*, 307–324.
(4) Mukerjee, S.; Urian, R. C.; Lee, S. J.; Ticianelli, E. A.; McBreen, J. Electrocatalysis of Co Tolerance by Carbon-Supported Ptmo Electrocatalysts in PEMFCs. *J. Electrochem. Soc.* **2004**, *151*, A1094–A1103.
(5) Ehteshami, S. M. M.; Jia, Q.; Halder, A.; Chan, S. H.; Mukerjee, S. The Role of Electronic Properties of Pt and Pt Alloys for Enhanced Reformate Electro-Oxidation in Polymer Electrolyte Membrane Fuel Cells. *Electrochim. Acta* **2013**, *107*, 155–163.
(6) Birry, L.; Lasia, A. Studies of the Hydrogen Evolution Reaction on Raney Nickel—Molybdenum Electrodes. *J. Appl. Electrochem.* **2004**, *34*, 735–749.
(7) McKone, J. R.; Sadtler, B. F.; Werlang, C. A.; Lewis, N. S.; Gray, H. B. Ni–Mo Nanopowders for Efficient Electrochemical Hydrogen Evolution. *ACS Catal.* **2012**, *3*, 166–169.
(8) Miousse, D.; Lasia, A.; Borck, V. Hydrogen Evolution Reaction on Ni-Al-Mo and Ni-Al Electrodes Prepared by Low Pressure Plasma Spraying. *J. Appl. Electrochem.* **1995**, *25*, 592–602.
(9) Pourbaix, M. *Atlas of Electrochemical Equilibria in Aqueous Solutions*; Pergamon Press: Brussels, 1966.
(10) Xiao, L.; Zhang, S.; Pan, J.; Yang, C.; He, M.; Zhuang, L.; Lu, J. First Implementation of Alkaline Polymer Electrolyte Water Electrolysis Working Only with Pure Water. *Energy Env. Sci.* **2012**, *5*, 7869–7871.
(11) Brown, D. E.; Mahmood, M. N.; Man, M. C. M.; Turner, A. K. Preparation and Characterization of Low Overvoltage Transition Metal Alloy Electrocatalysts for Hydrogen Evolution in Alkaline Solutions. *Electrochim. Acta* **1984**, *29*, 1551–1556.
(12) Bagotzky, V. S.; Osetrova, N. V. Investigations of Hydrogen Ionization on Platinum with the Help of Micro-Electrodes. *J. Electroanal. Chem. Interfac.* **1973**, *43*, 233–249.
(13) Sheng, W.; Gasteiger, H. A.; Shao-Horn, Y. Hydrogen Oxidation and Evolution Reaction Kinetics on Platinum: Acid Vs Alkaline Electrolytes. *J. Electrochem. Soc.* **2010**, *157*, B1529–B1536.
(14) Subbaraman, R.; Tripkovic, D.; Strmcnik, D.; Chang, K.-C.; Uchimura, M.; Paulikas, A. P.; Stamenkovic, V.; Markovic, N. M. Enhancing Hydrogen Evolution Activity in Water Splitting by Tailoring Li^+-$Ni(OH)_2$-Pt Interfaces. *Science* **2011**, *334*, 1256–1260.
(15) Kendrick, I.; Kumari, D.; Yakaboski, A.; Dimakis, N.; Smotkin, E. S. Elucidating the Ionomer-Electrified Metal Interface. *J. Am. Chem. Soc.* **2010**, *132*, 17611–17616.
(16) Zhang, H.; Shen, P. K. Recent Development of Polymer Electrolyte Membranes for Fuel Cells. *Chem. Rev.* **2012**, *112*, 2780–2832.
(17) Pan, J.; Chen, C.; Zhuang, L.; Lu, J. Designing Advanced Alkaline Polymer Electrolytes for Fuel Cell Applications. *Acc. Chem. Res.* **2011**, *45*, 473–481.
(18) Li, N.; Leng, Y.; Hickner, M. A.; Wang, C.-Y. Highly Stable, Anion Conductive, Comb-Shaped Copolymers for Alkaline Fuel Cells. *J. Am. Chem. Soc.* **2013**, *135*, 10124–10133.
(19) Ünlü, M.; Abbott, D.; Ramaswamy, N.; Ren, X.; Mukerjee, S.; Kohl, P. A. Analysis of Double Layer and Adsorption Effects at the Alkaline Polymer Electrolyte-Electrode Interface. *J. Electrochem. Soc.* **2011**, *158*, B1423–B1431.
(20) Spendelow, J. S.; Wieckowski, A. Electrocatalysis of Oxygen Reduction and Small Alcohol Oxidation in Alkaline Media. *Phys. Chem. Chem. Phys.* **2007**, *9*, 2654–2675.
(21) Ramaswamy, N.; Mukerjee, S. Fundamental Mechanistic Understanding of Electrocatalysis of Oxygen Reduction on Pt and Non-Pt Surfaces: Acid Versus Alkaline Media. *Adv. Phys. Chem.* **2012**, *2012*, 17.
(22) Gong, M.; Li, Y.; Wang, H.; Liang, Y.; Wu, J. Z.; Zhou, J.; Wang, J.; Regier, T.; Wei, F.; Dai, H. An Advanced Ni–Fe Layered Double Hydroxide Electrocatalyst for Water Oxidation. *J. Am. Chem. Soc.* **2013**, *135*, 8452–8455.
(23) Li, X.; Walsh, F. C.; Pletcher, D. Nickel Based Electrocatalysts for Oxygen Evolution in High Current Density, Alkaline Water Electrolysers. *Phys. Chem. Chem. Phys.* **2011**, *13*, 1162–1167.
(24) Hu, Q.; Li, G.; Pan, J.; Tan, L.; Lu, J.; Zhuang, L. Alkaline Polymer Electrolyte Fuel Cell with Ni-Based Anode and Co-Based Cathode. *Int. J. Hydrogen Energy* **2013**, *38*, 16264–16268.
(25) Lu, S.; Pan, J.; Huang, A.; Zhuang, L.; Lu, J. Alkaline Polymer Electrolyte Fuel Cells Completely Free from Noble Metal Catalysts. *Proc. Nat. Acad. Sci.* **2008**, *105*, 20611–20614.

DOI: 10.1021/jp512311c
J. Phys. Chem. C 2015, 119, 5467–5477

(26) Danilovic, N.; Subbaraman, R.; Strmcnik, D.; Paulikas, A. P.; Myers, D.; Stamenkovic, V. R.; Markovic, N. M. The Effect of Noncovalent Interactions on the HOR, ORR, and HER on Ru, Ir, and $Ru_{0.50}Ir_{0.50}$ Metal Surfaces in Alkaline Environments. *Electrocatalysis* **2012**, *3*, 221−229.
(27) Strmcnik, D.; Uchimura, M.; Wang, C.; Subbaraman, R.; Danilovic, N.; van der, V.; Paulikas, A. P.; Stamenkovic, V. R.; Markovic, N. M. Improving the Hydrogen Oxidation Reaction Rate by Promotion of Hydroxyl Adsorption. *Nat. Chem.* **2013**, *5*, 300−306.
(28) Markovic, N.; Gasteiger, H.; Ross, P. N. Kinetics of Oxygen Reduction on Pt(Hkl) Electrodes: Implications for the Crystallite Size Effect with Supported Pt Electrocatalysts. *J. Electrochem. Soc.* **1997**, *144*, 1591−1597.
(29) Markovića, N. M.; Sarraf, S. T.; Gasteiger, H. A.; Ross, P. N. Hydrogen Electrochemistry on Platinum Low-Index Single-Crystal Surfaces in Alkaline Solution. *J. Chem. Soc., Faraday Trans.* **1996**, *92*, 3719−3725.
(30) Böckris, J.; Reddy, A.; Gamboa-Aldeco, M. *Modern Electrochemistry, 2A: Fundamentals of Electrodics*; Springer US: New York, 2000.
(31) Jakšić, J. M.; Vojnović, M. V.; Krstajić, N. V. Kinetic Analysis of Hydrogen Evolution at Ni−Mo Alloy Electrodes. *Electrochim. Acta* **2000**, *45*, 4151−4158.
(32) Soares, D. M.; Teschke, O.; Torriani, I. Hydride Effect on the Kinetics of the Hydrogen Evolution Reaction on Nickel Cathodes in Alkaline Media. *J. Electrochem. Soc.* **1992**, *139*, 98−105.
(33) Mauer, A. E.; Kirk, D. W.; Thorpe, S. J. The Role of Iron in the Prevention of Nickel Electrode Deactivation in Alkaline Electrolysis. *Electrochim. Acta* **2007**, *52*, 3505−3509.
(34) Danilovic, N.; Subbaraman, R.; Strmcnik, D.; Chang, K.-C.; Paulikas, A. P.; Stamenkovic, V. R.; Markovic, N. M. Enhancing the Alkaline Hydrogen Evolution Reaction Activity through the Bifunctionality of $Ni(OH)_2$/Metal Catalysts. *Angew. Chem., Int. Ed.* **2012**, *51*, 12495−12498.
(35) Subbaraman, R.; Tripkovic, D.; Chang, K.-C.; Strmcnik, D.; Paulikas, A. P.; Hirunsit, P.; Chan, M.; Greeley, J.; Stamenkovic, V.; Markovic, N. M. Trends in Activity for the Water Electrolyser Reactions on 3d M(Ni,Co,Fe,Mn) Hydr(Oxy)Oxide Catalysts. *Nat. Mater.* **2012**, *11*, 550−557.
(36) Subbaraman, R.; Tripkovic, D.; Strmcnik, D.; Chang, K.-C.; Uchimura, M.; Paulikas, A. P.; Stamenkovic, V.; Markovic, N. M. Enhancing Hydrogen Evolution Activity in Water Splitting by Tailoring Li^+-$Ni(OH)_2$-Pt Interfaces. *Science* **2011**, *334*, 1256−1260.
(37) Jaksic, J. M.; Labou, D.; Papakonstantinou, G. D.; Siokou, A.; Jaksic, M. M. Novel Spillover Interrelating Reversible Electrocatalysts for Oxygen and Hydrogen Electrode Reactions. *J. Phys. Chem. C* **2010**, *114*, 18298−18312.
(38) Jaksic, M. M.; Botton, G. A.; Papakonstantinou, G. D.; Nan, F.; Jaksic, J. M. Primary Oxide Latent Storage and Spillover Enabling Electrocatalysts with Reversible Oxygen Electrode Properties and the Alterpolar Revertible (Pemfc Versus We) Cell. *J. Phys. Chem. C* **2014**, *118*, 8723−8746.
(39) Santos, E.; Quaino, P.; Schmickler, W. Theory of Electrocatalysis: Hydrogen Evolution and More. *Phys. Chem. Chem. Phys.* **2012**, *14*, 11224−11233.
(40) Hall, D. S.; Bock, C.; MacDougall, B. R. The Electrochemistry of Metallic Nickel: Oxides, Hydroxides, Hydrides and Alkaline Hydrogen Evolution. *J. Electrochem. Soc.* **2013**, *160*, F235−F243.
(41) Hitz, C.; Lasia, A. Experimental Study and Modeling of Impedance of the Her on Porous Ni Electrodes. *J. Electroanal. Chem.* **2001**, *500*, 213−222.
(42) Lasia, A.; Rami, A. Kinetics of Hydrogen Evolution on Nickel Electrodes. *J. Electroanal. Chem. Interfac.* **1990**, *294*, 123−141.
(43) Stoia, M.; Stefanescu, M.; Barbu, M.; Barvinschi, P.; Barbu-Tudoran, L. Studies Regarding the Formation from Metal Nitrates and Diol of $NiM_2^{III}O_4$ Spinels, inside a Silica Matrix. *J. Therm. Anal. Calorim.* **2012**, *108*, 1041−1049.
(44) Ştefănescu, M.; Barbu, M.; Barvinschi, P.; Ştefănescu, O. The Obtaining of $NiCr_2O_4$ Nanoparticles by Unconventional Synthesis Methods. *J. Therm. Anal. Calorim.* **2013**, *111*, 1121−1127.
(45) Cheng, X.-d.; Min, J.; Zhu, Z.-q.; Ye, W.-p. Preparation of High Emissivity $NiCr_2O_4$ Powders with a Spinel Structure by Spray Drying. *Int. J. Miner Metal. Mater.* **2012**, *19*, 173−178.
(46) Greskovich, C. Kinetics of $NiCr_2O_4$ Formation and Diffusion of Cr^{3+} Ions in NiO. *J. Am. Ceram. Soc.* **1970**, *53*, 498−502.
(47) Gassan-Zadeh, G. Z.; Woode, M. Y.; Alkhazov, T. G. Effect of Oxygen on No Reduction over Nickel Chromite Catalysts. *React. Kinet. Catal. Lett.* **1988**, *36*, 33−37.
(48) Simentsova, I. I.; Minyukova, T. P.; Khassin, A. A.; Dokuchits, E. V.; Davydova, L. P.; Molina, I. Y.; Plyasova, L. M.; Kustova, G. N.; Yurieva, T. M. The Effect of the Precursor Structure on the Catalytic Properties of the Nickel−Chromium Catalysts of Hydrogenation Reactions. *Russ Chem. Bull.* **2010**, *59*, 2055−2060.
(49) Ren, Y.; Bruce, P. G.; Ma, Z. Solid-Solid Conversion of Ordered Crystalline Mesoporous Metal Oxides under Reducing Atmosphere. *J. Mater. Chem.* **2011**, *21*, 9312−9318.
(50) Gong, M., et al. Nanoscale Nickel Oxide/Nickel Heterostructures for Active Hydrogen Evolution Electrocatalysis. *Nat. Commun.* **2014**, *5*.

DOI: 10.1021/jp512311c
J. Phys. Chem. C 2015, 119, 5467−5477